

Research Paper

Ultra-small pH-responsive Nd-doped NaDyF₄ Nanoagents for Enhanced Cancer Theranostic by *in situ* Aggregation

Yuxin Liu^{1*}, Huimin Fan^{1*}, Quanwei Guo¹, Anqi Jiang¹, Xiaoxia Du², Jing Zhou¹✉

1. Department of Chemistry, Capital Normal University, Beijing, 100048, P. R. China;

2. Shanghai Key Laboratory of Magnetic Resonance, Physics Department, East China Normal University, Shanghai 200062, P. R. China.

* These authors contributed equally to this work.

✉ Corresponding author: jingzhou@cnu.edu.cn (J. Zhou)

© Ivyspring International Publisher. This is an open access article distributed under the terms of the Creative Commons Attribution (CC BY-NC) license (<https://creativecommons.org/licenses/by-nc/4.0/>). See <http://ivyspring.com/terms> for full terms and conditions.

Received: 2017.06.21; Accepted: 2017.07.12; Published: 2017.09.26

Abstract

To achieve accurate tumor location and highly efficient cancer therapy effect, the properties of cancer theranostic agents should be optimized and enhanced. In this work, ultra-small Nd doped NaDyF₄ were firstly reported as novel contrast agents for near-infrared second window downconversion luminescence (NIR II DCL) and magnetic resonance imaging. Based on the optimization strategy, gallic acid-Fe(III) complex modified NaDyF₄:10%Nd (NaDyF₄:10%Nd-GA-Fe) was selected as the optimal agent with high transversal relaxivity, strong NIR II DCL, high photothermal conversion efficiency, and low toxicity. *In vitro* experiment found that it can be aggregated rapidly in low pH condition, leading to the particle size increasing. Due to the theranostic properties coupled in NaDyF₄:10%Nd-GA-Fe are size dependent, properties enhancement was observed within the pH responsive aggregation progress. Further study in small animal model bearing tumor demonstrated the enhanced cancer theranostic by *in situ* aggregation. The optimized nanoagents have potential applications in medical and also provide a novel strategy for future study of cancer theranostic enhancement.

Key words: neodymium, NaDyF₄, NIR II, magnetic resonance imaging, photothermal therapy.

Introduction

Meeting the requirement of real-time diagnosis, luminescence imaging recently became the research hotspot¹. With fascinating and unique properties, rare earth elements have a great reputation in this domain, which lead to the wide and deep exploration in lanthanide doped nanomaterials to develop high efficient agents for luminescence imaging^{2,3}. Since biological tissues has an "optical transparency window" in near-infrared second window (NIR II) region, NIR II luminescence imaging take the advantage of deep tissue penetration, reduced photo-damage effects, low photo-scattering, and high signal-to-noise ratio in turn⁴⁻⁶. Recently, a brilliant strategy was come up, applying neodymium (Nd) as

novel sensitizer which can be excited by 808 nm laser and emitted in NIR II region^{7,8}. Thanks to the long excitation and emission wavelength, Nd doped nanomaterials as NIR II downconversion luminescent (DCL) agents have the potential application in accurate real-time cancer diagnosis.

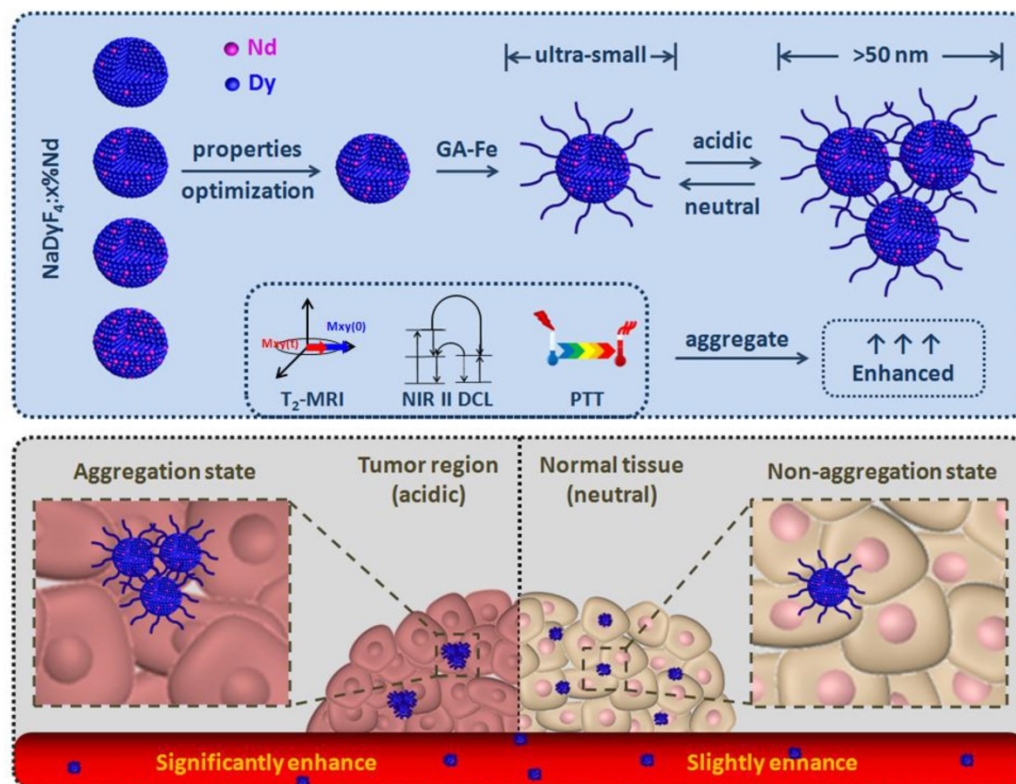
However, many works pointed out that luminescence imaging still have limitation in low tissue resolution^{9,10}. Thence, developing multifunctional luminescence agents coupled with high resolution imaging should be considered as priority. Among the imaging methods, T₂-weighted magnetic resonance imaging (MRI) is widely used in clinical cancer diagnosis and can provide high

resolution 3D images of pathological phenomena such as tumors and inflammation^{11,12}. Previous works suggested dysprosium (Dy) doped agents can be applied for effective T₂-weighted MRI *in vitro* and *in vivo*¹³⁻¹⁵. For cancer ablation following comprehensive diagnosis, photothermal therapy (PTT) is also a novel targeted and non-invasive therapeutic intervention for cancer treatment, which can be easily achieved by the combination of photothermal conversion agents and suitable irradiation in the cancerous area, thereby killing ordinary tumor cells at a relative high temperature (> 42°C)^{16,17}. Among all the discovered photothermal conversion agents, mainly including noble metals¹⁸⁻²⁰, semiconductors²¹⁻²⁴, molecular dyes²⁵⁻²⁷, conjugated polymers²⁸⁻³¹, and carbon-based materials³²⁻³⁴, the molecular dyes constitute the largest and most diverse family, which provide them with special performance in nanomaterial-based PTT³⁵. Therefore, it is necessary to explore multifunctional nanoagents with outstanding NIR II DCL imaging and T₂-weighted MRI properties, as well as photothermal therapeutic effect for cancer theranostic.

Apart from multifunction, the ultra-small hydrodiameter (sub 10 nm) was also required to avoid the accumulation in reticuloendothelial system, partly contributing to the long circulation time, high tumor accumulation amount, thus resulting in cancer theranostic improvement^{36,37}. However, the theranostic effect was still limited due to the small

size. Therefore, a strategy for theranostic properties improvement of the accumulated nanoagents in tumor region was needed to be put forward. Considering the fact that rare earth based luminescence, T₂-weighted MRI, and photothermal conversion properties were size dependent, developing a multifunctional nanoagent which can *in situ* aggregate in tumor region would seem to be a reasonable strategy for the cancer theranostic enhancement³⁸⁻⁴⁰. Since the tumor region was more acidic than normal tissues, the pH-induced *in situ* aggregation of the nanoagent in tumor region by aid of pH sensitive ligands was feasible for highly cancer theranostic enhancement.

In this work, we firstly reported a series of multifunctional NaDyF₄ nanoagents doped with different amount Nd for NIR II DCL imaging and T₂-weighted MRI, further discussing and optimizing their imaging properties. The optimized agent was then modified with photothermal conversion and pH-responsive gallic acid-Fe(III) complex (GA-Fe) and tested their pH induced theranostic properties enhancement. Following efforts have been directed towards treatment of tumor bearing-mice with the optimized GA-Fe modified nanoagents to illustrate their *in situ* aggregation-mediated enhanced theranostic effect and biosafety *in vitro* and *in vivo* (Scheme 1).



Scheme 1. Optimization of ultra-small NaDyF₄:x%Nd nanoagents for enhanced cancer theranostic by pH-responsive *in situ* aggregation.

Results and Discussion

Synthesis and characterization of NaDyF₄:x%Nd.

Hydrophobic oleic acid (OA) coated NaDyF₄:x%Nd ($x = 2.5, 5, 10, 20$) nanoagents were synthesized *via* a typical solvothermal method¹⁵. Transmission electron microscopy (TEM) images showed that the NaDyF₄:x%Nd nanoagents are well dispersed in cyclohexane with good crystallinity and uniform shape (Figure 1A-D). All samples exhibit a narrow size distribution (6.6 ± 1.3 nm). The unobvious size change through Nd dopant may be interpreted to

the low dopant amount and ultra-small size. The energy-dispersive X-ray analysis (EDXA) spectra and ICP-MS of the NaDyF₄ nanoagents confirmed the exclusive composition of Na, Dy, and F (Figure S1 and Table S1), which indicated the element formation of Nd doped NaDyF₄ nanoagents. High-resolution TEM (HR-TEM) images and powder X-ray diffraction (XRD) patterns of NaDyF₄:x%Nd nanoagents showed good crystallinity and confirmed their hexagonal phase (JCPDS: 027-0687 for NaDyF₄ and JCPDS: 35-1367 for NaNdF₄) (Figure S2). Selected area electron diffraction (SAED) pattern could also support this observation (Figure S3).

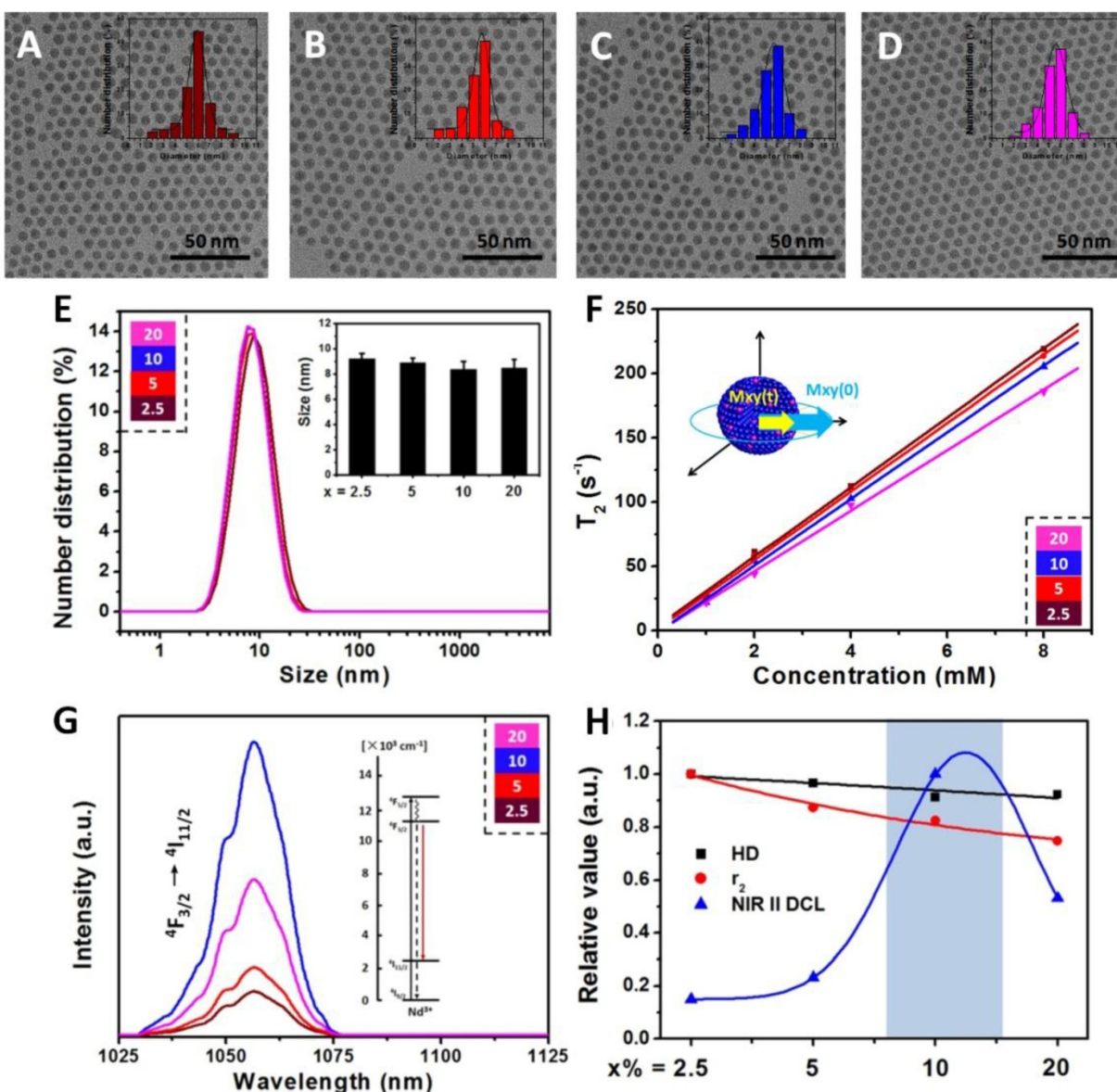


Figure 1. Characterizations and optimization of NaDyF₄:x%Nd ($x = 2.5, 5, 10, 20$) nanoagents. TEM images A-D) of hydrophobic NaDyF₄:x%Nd ($x = 2.5, 5, 10, 20$) nanoagents (Insert: size distribution of NaDyF₄:x%Nd). Hydrodiameter E), transversal relaxivity (r_2) F), and NIR II DCL G) properties of hydrophilic NaDyF₄:x%Nd ($x = 2.5, 5, 10, 20$) nanoagents. The properties variation H) as a function of Nd concentration in obtained nanoagents (HD: the abbreviation of hydrodiameter; NIR II DCL: the NIR II DCL intensity under 808 laser irradiation with power intensity of 4.5 W cm^{-2}). These results confirmed the successful controlled synthesis of ultra-small hexagonal phase NaDyF₄:x%Nd ($x = 2.5, 5, 10, 20$) nanoagents and demonstrated that the 10% Nd doped NaDyF₄ was preferred for further modification and applications.

Optimization of pH-responsive multifunctional nanoagents

Multifunctional imaging properties optimization

To obtain the hydrophilic $\text{NaDyF}_4:x\%\text{Nd}$ for further application, nanoagents were treated using nitrosoniumtetrafluoroborate (NOBF_4) to remove OA ligands on the surface, and gallic acid (GA) was then used to coat the four types of ligand-free nanoagents. Fourier transform infrared (FTIR) spectra proved the successful ligand exchange (Figure S4). Zeta potential investigation and dynamic light scattering (DLS) measurement suggested that all the four type nanoagents can well dispersed in water with a similar average hydrodiameter (HD) (Figure 1E).

The water-dispersible $\text{NaDyF}_4:x\%\text{Nd}$ nanoagents were then investigated for positive longitudinal relaxivity (r_1) and negative transverse relaxivity (r_2) measurements, which were measured as a function of nanoagents molar concentrations at room temperature using a 3 T magnetic resonance imaging (MRI) system. All $\text{NaDyF}_4:x\%\text{Nd}$ nanoagents showed good r_2 enhancement and relative low r_1 as a result of the presence of the Dy^{3+} ions (Figure 1F and Figure S5). As the Nd^{3+} dopant amount increasing, r_2/r_1 of $\text{NaDyF}_4:x\%\text{Nd}$ decreased monotonously and surprisingly showed a linear relationship (Figure S6). Then, the near-infrared second window downconversion luminescence (NIR II DCL) was also taken into comparison. The NIR II DCL emission can be ascribed to the f-f electronic transition of Nd^{3+} . Upon 808 nm excitation, DCL emission peaks of Nd in the NIR II region occurred at 1050 nm and 1330 nm, which correspond to the transition from ${}^4\text{F}_{3/2} \rightarrow {}^4\text{I}_{11/2}$ and ${}^4\text{F}_{3/2} \rightarrow {}^4\text{I}_{13/2}$. (Figure 1G and Figure S7). The interplay between both Nd concentration-induced absorption increment and concentration-induced luminescence quenching result in the max NIR emission peak at 10% Nd dopant amount. Nevertheless, with continuous increasing of Nd doping amount (>13%), the cross-relaxation would lead to the luminescence quenching accordingly. $\text{NaDyF}_4:10\%\text{Nd}$ has a similar quantum yield of ~19.4% with previous work (~22% for $\text{NaGdF}_4:3\%\text{Nd}$) and the different optimized Nd concentration may be contributed to the various hosts, which influenced the surrounding of Nd and their optical properties by crystal field⁴¹. Since the luminescence intensity at 1050 nm was much stronger than that at 1330 nm, we then chose the 1050 nm luminescence for further study and imaging application. Considering all the factors above, $\text{NaDyF}_4:10\%\text{Nd}$ among the four nanoagents has a preferable MR and NIR II DCL imaging effect, which can be optimized for the further study (Figure 1H).

pH-responsive aggregation and properties enhancement

Gallic acid-Fe(III) complex (GA-Fe) has strong absorption at the range of 500-700 nm, and shows pH-responsive properties which can be efficiently aggregated in acidic condition (tumor region). The aggregation property of nanoagents may contribute to the protonation of modified GA-Fe(III) and the formation of hydrogen bond between oxygen atoms in hydroxyl groups and carboxyl groups according to previous report⁴². Hence, GA-Fe modified optimized $\text{NaDyF}_4:10\%\text{Nd}$ nanoagents ($\text{NaDyF}_4:10\%\text{Nd-GA-Fe}$) can be expected to be photothermal agents and enhance cancer theranostic effect.

First, the $\text{NaDyF}_4:10\%\text{Nd-GA-Fe}$ was synthesized and characterized (Figure S8,9). Due to the separation of GA-Fe absorption wavelength (500-700 nm) and $\text{NaDyF}_4:10\%\text{Nd}$ emission wavelength (1050 ± 25 nm), the GA-Fe modification has no obvious re-absorption effect on NIR II DCL of $\text{NaDyF}_4:10\%\text{Nd}$, which can ensure the efficiency of DCL imaging (Figure S9). The $\text{NaDyF}_4:10\%\text{Nd-GA-Fe}$ can be well dispersed with a small hydrodiameter of 8.7 ± 0.9 nm and zeta potential of -28.47 mV. It also shows a similar absorption as reported free GA-Fe complex (Figure S10). Then, we studied the aggregation and enhancement effect under different pH condition (pH = 4.5-7.5). TEM and DLS analysis showed an increasing of the average size of $\text{NaDyF}_4:10\%\text{Nd-GA-Fe}$ from 6.5 ± 0.7 nm (HD: 8.7 ± 0.9 nm) to 50.4 ± 4.4 nm (HD: 59.3 ± 6.6 nm) in acidic condition (pH = 4.5) and no obvious aggregation was observed in neutral condition (pH = 7.5) within 30 min (Figure 2A, B, D, E). Besides, relative high concentration of $\text{NaDyF}_4:10\%\text{Nd-GA-Fe}$ showed more rapid aggregation than low concentration, which can be explained as the easy attachment of nanoparticles in high concentration solution (Figure 2F). These results suggest that $\text{NaDyF}_4:10\%\text{Nd-GA-Fe}$ can efficiently aggregate under acidic condition. Notably, the aggregation-decomposition progress can be repeated by changing the pH condition (Figure 2C). After five circle of aggregation-decomposition progress, $\text{NaDyF}_4:10\%\text{Nd-GA-Fe}$ can still show good solubility and small HD (<10 nm) in solution (Figure 2G).

Besides, the ultraviolet-visible-near infrared (UV-vis-NIR) spectra also provide the same consequence by an obvious increase of absorption in low pH condition (Figure 3A). Because the aggregation of nanoagents increase the average size and further increase the molar extinction coefficient (ϵ value), the photothermal conversion effect of $\text{NaDyF}_4:10\%\text{Nd-GA-Fe}$ under different pH condition was calculated using the following equation.

$$\varepsilon = \frac{AV_{\text{NPs}}\rho N_A}{LC} \quad (1)$$

According to equation 1 and equation S1, the ε value of NaDyF₄:10%Nd-GA-Fe was increasing from 1.89×10^6 to $1.37 \times 10^8 \text{ M}^{-1} \text{ cm}^{-1}$ with the pH decreasing from 7.5 to 4.5, monotonously. The photothermal conversion efficiency (η value) of NaDyF₄:10%Nd-GA-Fe ($200 \mu\text{g mL}^{-1}$) under the pH = 4.5 condition was calculated using the following equation.

$$\eta = \frac{hA\Delta T_{\text{max}} - Q_s}{I(1 - 10^{-A})} \quad (2)$$

According to equation 2 and equation S2, the η value of the NaDyF₄:10%Nd-GA-Fe is 60.12%, which

is much higher than that of recently reported photothermal coupling agents (47.83% for rGO-Bi₂S₃, 36.10% for SnS) (Figure S11)^{43,44}. Moreover, the enhancement of diagnosis signals was also studied. With the condition turned from neutral to acidic, the T₂-weighted MRI and NIR II DCL signal intensity can be efficiently increased, which proved that NaDyF₄:10%Nd-GA-Fe can be used for enhanced cancer theranostic (Figure 3E-H). The increasing of MRI and NIR II DCL property may contribute to the decrease of surface area, which result in the weakening of spin-canting effect and surface quenching effect.

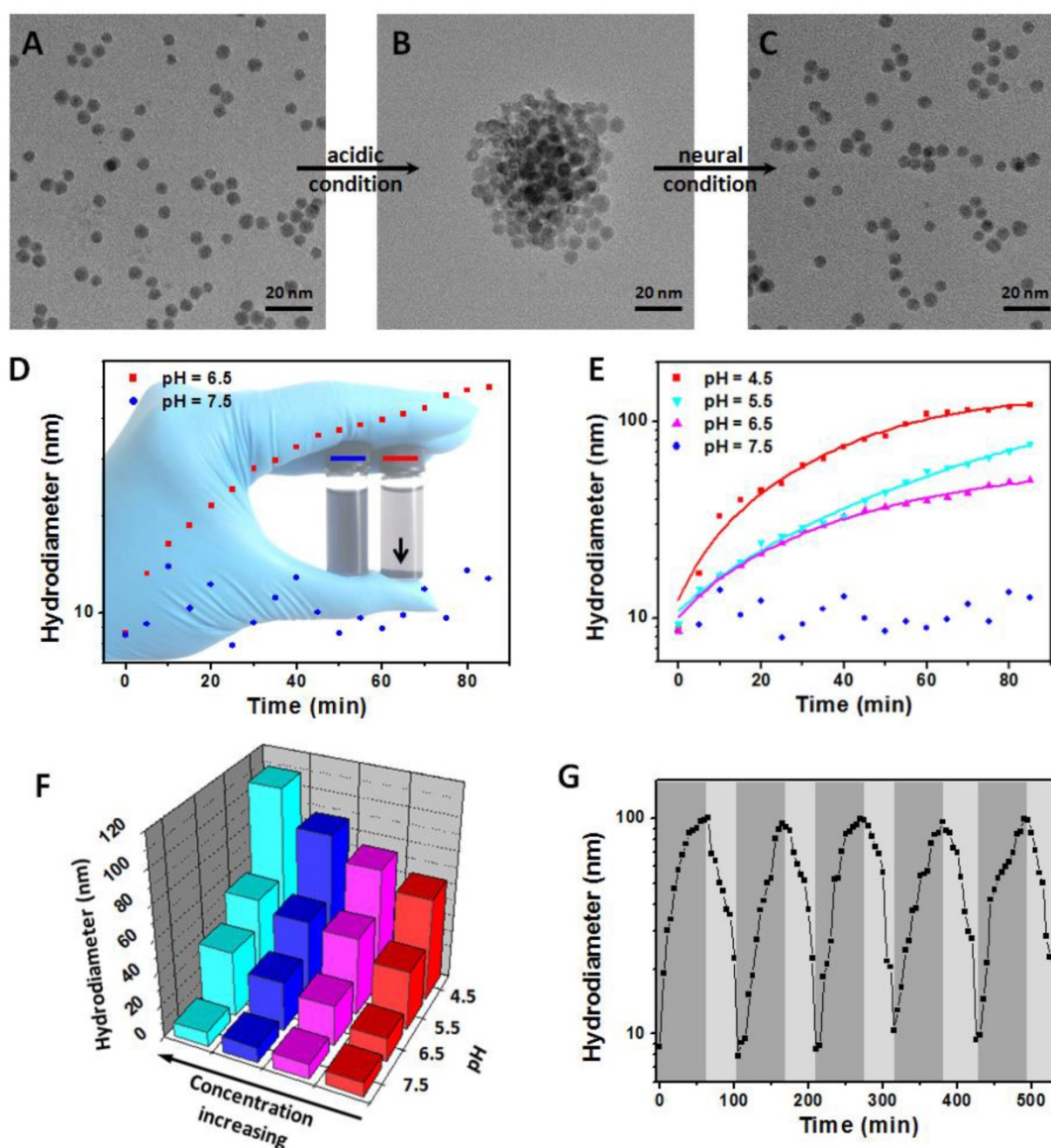


Figure 2. pH-induced aggregation-decomposition progress of NaDyF₄:10%Nd-GA-Fe. A-C) TEM images of NaDyF₄:10%Nd-GA-Fe in aggregation-decomposition progress. D,E) Hydrodiameter vs time plots of NaDyF₄:10%Nd-GA-Fe under different pH condition. F) Hydrodiameter vs concentration and pH plots of NaDyF₄:10%Nd-GA-Fe. G) Hydrodiameter variations of NaDyF₄:10%Nd-GA-Fe under the different pH condition for five cycles. These results suggested NaDyF₄:10%Nd-GA-Fe can response to different pH condition and hence aggregate in acidic condition.

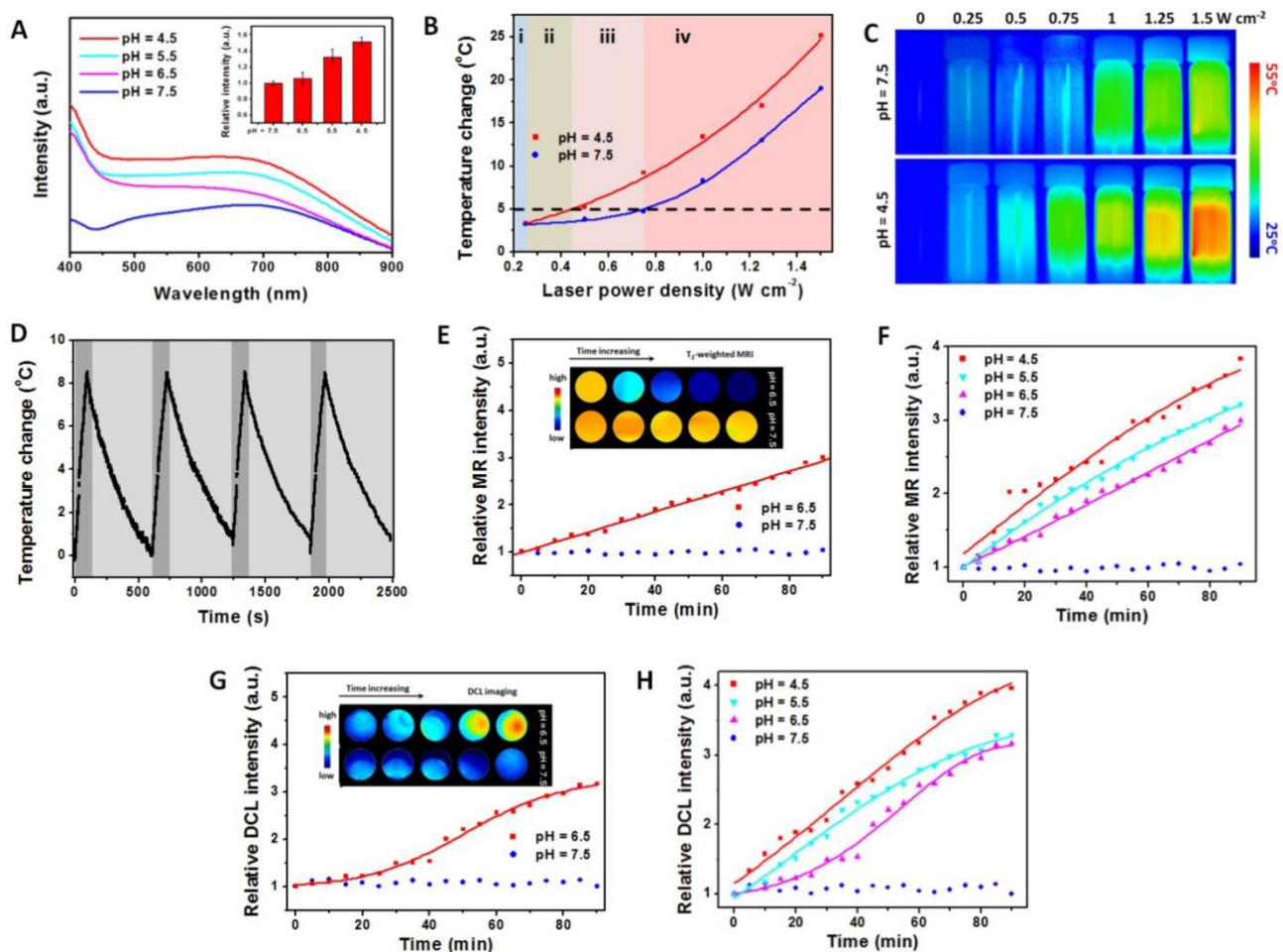


Figure 3. pH-induced properties enhancement of NaDyF₄:10%Nd-GA-Fe. A) UV-vis-NIR spectra of NaDyF₄:10%Nd-GA-Fe under different pH condition within 30 min (pH = 4.5, 5.5, 6.5, and 7.5). Inset: relative intensity at 808 nm. Photothermal temperature change B) and photothermal images C) of NaDyF₄:10%Nd-GA-Fe under laser irradiation with different power intensity. D) Temperature variations of NaDyF₄:10%Nd-GA-Fe (200 ppm) under the continuous irradiations of 808 nm laser for four cycles. E,F) Relative MR intensity vs time plots of NaDyF₄:10%Nd-GA-Fe under different pH condition (Inset: MRI images in tube). G,H) Relative DCL intensity vs time plots of NaDyF₄:10%Nd-GA-Fe under different pH condition (Inset: NIR II DCL images in tube). These results suggested NaDyF₄:10%Nd-GA-Fe has enhanced properties in acidic condition and the potential to achieve enhanced cancer theranostic.

The stability of NaDyF₄:10%Nd-GA-Fe was also investigated. UV-vis-NIR spectra and DLS of NaDyF₄:10%Nd-GA-Fe after several days standing and after several hours irradiation were measured, and suggested great stability under neutral condition and different biological solution (Figure S12, Table S2, S3). Inductively coupled plasma mass spectrometry (ICP-MS) results suggested that no noticeable Fe(III) and Dy (III) leaching from NaDyF₄:10%Nd-GA-Fe after 60 days standing or 1 hour irradiation in both neutral and acidic condition. It was also found that NaDyF₄:10%Nd-GA-Fe was a robust photothermal heater after five cycles of NIR laser-induced heating (Figure 3D). In all, the pH-responsive enhanced multifunctional properties and stability of NaDyF₄:10%Nd-GA-Fe nanocomposites make them superior as a promising pH-responsive multifunctional agent for enhanced cancer theranostic.

Power density optimization

Since the body temperature of human beings was ~37°C and the temperature over 42°C may increase the potential risk of overheat to normal tissues, temperature change less than 5°C will provide a safe condition for cancer diagnosis. To avoid the potential damage to normal tissues during the cancer diagnosis and obtain a high photothermal temperature change during the cancer therapy, the power density of irradiation laser was also optimized (Figure 3B, C). When the power density was 0.25 W cm⁻² or lower, there are no obvious temperature increase (<3°C), and thus NIR II DCL imaging can be performed under this power density stage (Figure 3B i). More importantly, the temperature change was lower than 5°C under 0.25-0.44 W cm⁻² and can show a significant difference between acidic condition and neutral condition. Hence, the power intensity range

guarantees the safety of photothermal imaging (Figure 3I ii). While the power intensity increased to the range of 0.44-0.74 W cm⁻², the temperature can increase by over 5°C in acidic condition and only by less than 5°C in neural condition, which suggested that the suitable laser power intensity range can both ensure the therapeutic effect and reduce the heat threaten to normal tissue (Figure 3B iii). Under the power intensity >0.74 W cm⁻², the temperature change can achieved over 5°C in both the acidic and neural condition, which may cause potential damage risk and hence not suitable for photothermal therapy (PTT) (Figure 3B iv). The low temperature change would lead to cell death, but the surviving cells would have the capacity to resistant further heat damage by activating the heat-shock proteins. Meanwhile, the high temperature can result in irreversible injury, by accelerating biological reaction and biomeleculc damage. Therefore, the nanoagents would show high cytotoxicity under acidic condition rather than neutral condition. This result suggested that the using of 808 nm laser with different power density can both ensure the cancer diagnosis safety and the theranostic effect.

Cancer theranostic enhancement *in vitro* and *in vivo*

T₂-weighted MR image can reveal pathological phenomena and high-resolution 3D images, which would be benefit to the location of tumor¹¹. Luminescence imaging achieves dynamic real-time imaging to monitor the ablation of tumor and photothermal images are used to record the real-time temperature change^{45,46}. Therefore, the combination of imaging modalities can provide complementary information in cancer theranostic. To confirm the potential application of NaDyF₄:10%Nd-GA-Fe as a multifunctional imaging probe and show enhanced imaging effect in tumor region than normal tissue, a series of *in vitro* and *in vivo* experiments were carried out. A typical non-pH-responsive citric acid-Fe (III) complex modified NaDyF₄:10%Nd (NaDyF₄:10%Nd-CA-Fe, HD: 9.1 nm, zeta potential: -27.60 mV) with similar imaging properties was designed and optimized for comparison (Figure S13).

To demonstrate the feasibility of NaDyF₄:10%Nd-GA-Fe as an enhanced multimodal imaging probe, we firstly compared the T₂-weighted MRI *in vitro*. In comparison with in neutral condition, NaDyF₄:10%Nd-GA-Fe in acidic condition showed a sharper contrast and NaDyF₄:10%Nd-CA-Fe showed no obvious difference between those two conditions (Figure 4A). Further study was taken on HCT116 tumor-bearing mice model. Post-injection T₂-weighted MRI images at 0 and 120 min showed clearly contrast in the tumor region, which illustrated

the possibility as a T₂-weighted MRI contrast agent for bioapplication (Figure 4B). Besides, T₂-weighted MRI signals in tumor and liver region were measured 1 hour post-injection and the tumor/liver ratio from the MRI images were also calculated. The result suggested that mice receiving NaDyF₄:10%Nd-GA-Fe had much more obvious tumor/liver ratio change than NaDyF₄:10%Nd-CA-Fe (Figure S14). To further demonstrate the pH-induced T₂-weighted MRI enhancement *in vivo*, nanoagents was intratumorally (2 mg per kg body weight of mouse) injected to tumor-bearing mice, respectively. By intratumorous injection, mice receiving NaDyF₄:10%Nd-GA-Fe showed much more significant T₂-weighted MRI signal enhancement in tumor region than that receiving NaDyF₄:10%Nd-CA-Fe (Figure 4C). The same result was also found in NIR II DCL imaging (Figure 4D,E and Figure S15). The above results suggested that NaDyF₄:10%Nd-GA-Fe can selectively enhanced the MRI and NIR II DCL signal in tumor region due to the acidic microenvironment, which illustrated the pH-responsive enhanced cancer diagnosis by *in situ* aggregation progress *in vivo* (Figure S16).

Since NaDyF₄:10%Nd-GA-Fe possessed good solubility, stability, and photothermal conversion efficiency in biological aqueous media, it could be also considered as a photothermal therapeutic agent. NaDyF₄:10%Nd-GA-Fe under the laser irradiation with an optimized power intensity of 0.64 W cm⁻² showed enhanced photothermal therapeutic effect on cancerous cells (cell viability: <10%) compared to normal cells (cell viability: >75%) (Figure 4F). Considering the fact that NaDyF₄:10%Nd-GA-Fe has enhanced photothermal therapeutic effect in tumor cells and the thermal signal of tumors increased over time and showed an obvious contradistinction with surrounding tissue after NaDyF₄:10%Nd-GA-Fe injection (Figure 4G), PTT *in vivo* was further studied with several groups of HCT116 tumor-bearing mice. In the test group, mice were intravenously injected with a PBS solution of NaDyF₄:10%Nd-GA-Fe and irradiated by a 808 nm continuous laser (Material + Laser, n = 5). For comparison, mice without injection of NaDyF₄:10%Nd-GA-Fe (Laser, n = 5), without laser irradiation (Materials, n = 5), and without injection or laser irradiation were chosen as the control groups. Upon irradiation at 808 nm (0.64 W cm⁻²) for 6 min, the tumors of the test groups shrank within 9 days. After 11 days therapy period, the tumors were eliminated, with residual black scars and no obvious swollen parts, and the relative tumor volume (V/V₀) shrank to 0. In contrast, the V/V₀ of tumors in the control and blank groups showed rapid growth over time (Figure 4H). Besides, the bodyweight of mice

were also determined. Within the first 3 days, the mice in test group showed a decrease in bodyweight, which demonstrated the efficient ablation of tumor by PTT. However, their bodyweight increase rapidly in

the following 11 days, suggesting that the mice receiving PTT were in the recovery process from therapy and make a supplementary to the low toxicity of nanoagents (Figure S17).

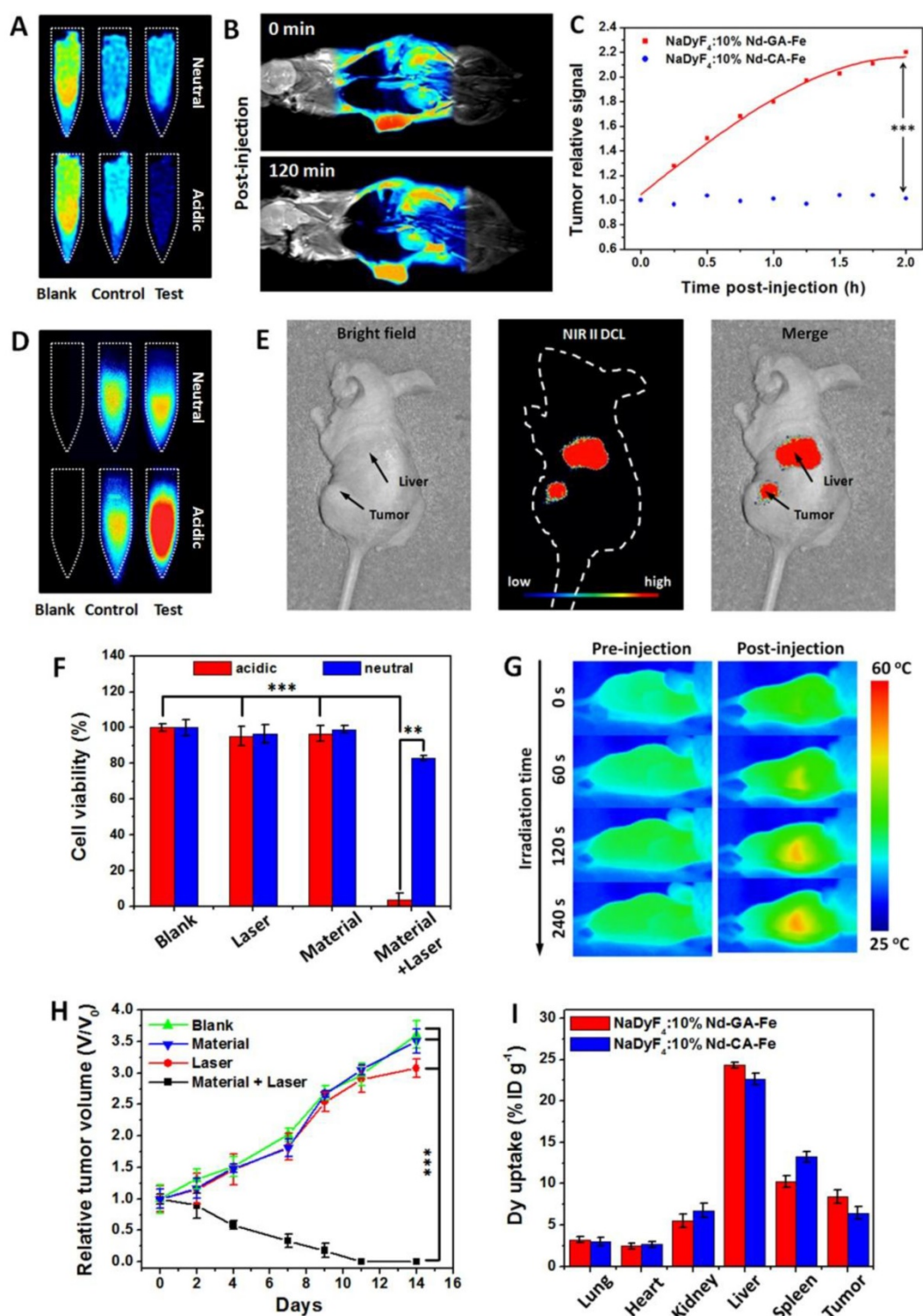


Figure 4. Enhanced cancer theranostics effect of NaDyF₄:10%Nd-GA-Fe in vitro and in vivo. T₂-weighted MRI images in pre- and post-incubated cells A) and tumor-bearing mice within 120 min post-injection B). C) T₂-weighted MRI signal in tumor region after intratumorous injection of NaDyF₄:10%Nd-GA-Fe. NIR II DCL images in pre- and post-incubated cells D) and tumor-bearing mice E). F) Photothermal therapy efficiency *in vitro*. G) Photothermal images in pre- and post-injection tumor-bearing mice. H) Tumor growth rates of test group (Material + Laser), control groups (Laser only, Materials only) and blank group (Blank). I) Tissue distribution of NaDyF₄:10%Nd-GA-Fe within 1 and 4 hour post-injection intravenously. NaDyF₄:10%Nd-CA-Fe was used for comparison (control in 4A and 4D). Statistical significance was determined from one-way t tests. Note: *p < 0.05, **p < 0.01, ***p < 0.001

The tissue distribution of both NaDyF₄:10%Nd-GA-Fe and NaDyF₄:10%Nd-CA-Fe was also quantitatively analyzed by ICP-MS and the Dy³⁺ is an indicator of the nanoagents which are not directly measured. Figure 4I shows that high dose of Dy³⁺ were uptake in both tumor region. These results demonstrated that the nanoagents can passive target and accumulate in the tumor region. More importantly, both of the nanoagents have a similar distribution in mice within 1 hour post-injection, indicating the cancer theranostic enhancement of NaDyF₄:10%Nd-GA-Fe in tumor-bearing mice model based on their pH responsive properties. Besides, the relatively long blood circulation half-live time was determined to be ~56 min benefit from their ultra-small HD. Thence, to sum up the points which we have just indicated, the NaDyF₄:10%Nd-GA-Fe can be applied to enhance cancer theranostic *in vitro* and *in vivo*.

Toxicity study

We then studied the *in vivo* toxicity of NaDyF₄:10%Nd-GA-Fe to determine the safety of bioapplication. A MTT assay shows no significant difference in proliferation of both HCT116 and CCC-HEL-1 cells in the absence or presence of NaDyF₄:10%Nd-GA-Fe (0-1.0 mg mL⁻¹) within 24 and 48 hours (Figure 5A,B). Cellular viabilities were estimated to over 85% even at high dose. The half maximal (50%) inhibitory concentration (IC₅₀) was also investigated *via* the MTT assay, and was calculated to be 3.97 mg mL⁻¹ (24 hours) and 3.19 mg mL⁻¹ (48 hours) for HCT116 cells, 3.94 mg mL⁻¹ (24 hours) and 3.42 mg mL⁻¹ (48 hours) for CCC-HEL-1 cells (Figure S18). The oxidation stress to HCT116 and CCC-HEL-1 cells was also determined by fluorescence method using singlet oxygen sensor green (SOSG). The result showed no obvious reactive oxygen species accumulation in both NaDyF₄:10%Nd-GA-Fe incubated HCT116 and CCC-HEL-1 cells, which suggested low oxidation stress of NaDyF₄:10%Nd-GA-Fe to cells (Figure S19). Moreover, healthy mice were injected intravenously with NaDyF₄:10%Nd-GA-Fe at the dose of 20 mg per kg body weight of mouse. Neither mouse death nor noticeable abnormal behavior was observed. Serum biochemistry assays and complete blood panel tests were carried out on NaDyF₄:10%Nd-GA-Fe-injected mice at 24 hours, 7 days, 30 days, and 60 days. The liver and kidney function indices, including alanine aminotransferase (ALT), aspartate aminotransferase (AST), total bilirubin (TBIL), albumin (ALB), total protein (TP), uric acid (UA) and creatinine (CREA) were all tested to be normal, which suggested no hepatic or kidney function influenced by

NaDyF₄:10%Nd-GA-Fe (Figure 5C-I). Besides, hematoxylin-eosin (H&E) stained tissues sections were also taken to testify histological examination, which suggested no appreciable adverse effect of NaDyF₄:10%Nd-GA-Fe to examined major organs, including liver, spleen, kidney, lung, and heart at 24 hours, 7 days, 30 days, and 60 days post-injection (Figure 5J). Dy amount in urine and feces was also determined by ICP-MS to study their metabolic pathway. The results suggested that NaDyF₄:10%Nd-GA-Fe can be rapidly metabolized by renal and fecal pathway (>80% within 48 hours), which greatly ensured their biosafety (Figure S20). Our results indicated that NaDyF₄:10%Nd-GA-Fe was nontoxic to mice at our tested dose.

Conclusions

In this work, we reported four types of ultra-small Nd doped NaDyF₄ nanoagents *via* typical solvothermal method. Considering their theranostic properties, NaDyF₄:10%Nd was optimized for further GA-Fe modification. The obtained NaDyF₄:10%Nd-Fe-GA exhibited high r_2 (27.9 mM⁻¹ s⁻¹), strong NIR II DCL (1050 nm and 1330 nm), outstanding photothermal conversion efficiency (60.12%), and unobservable toxicity. More importantly, the effective pH-responsibility properties make the nanoagents aggregate in acidic condition. Moreover, the *in vitro* and *in vivo* studies showed enhanced contrast in tumor region, which demonstrated that ultra-small NaDyF₄:10%Nd-Fe-GA has the potential to be applied in efficient cancer theranostic by pH-responsive *in situ* aggregation. Our results provided a novel optimization strategy of developing multifunctional nanoagents, as well as encouraged the further research in the subfield of cancer theranostic enhancement.

Experimental

Materials

Rare-earth oxides Nd₂O₃ (99.99%) and Dy₂O₃ (99.9%) were purchased from Beijing Lansu Co. China. Sodium hydroxide (NaOH), hydrochloride (HCl), ethanol, cyclohexane, and dichloromethane were purchased from Beijing Chemical Reagent Company. Oleic acid (OA) was purchased from Aldrich. 1-Octadecene (ODE), ammonium fluoride (NH₄F), and nitrosoniumtetrafluoroborate (NOBF₄) were purchased from Alfa Aesar Chemical (Tianjing) Co. Ltd. Iron (III) chloride (FeCl₃·6H₂O) was purchased from Thermo Fisher Scientific (China) Co Ltd. Gallic acid (GA) was purchased from Energy Chemical (Shanghai) Co. Ltd. Rare earth chlorides (LnCl₃, Ln: Nd, Dy) were prepared by dissolving the

corresponding metal oxide in HCl solution at elevated temperature and then evaporating the water completely under reduced pressure. All other

chemical reagents were of analytical grade and were used directly without further purification. Deionized (DI) water was used throughout.

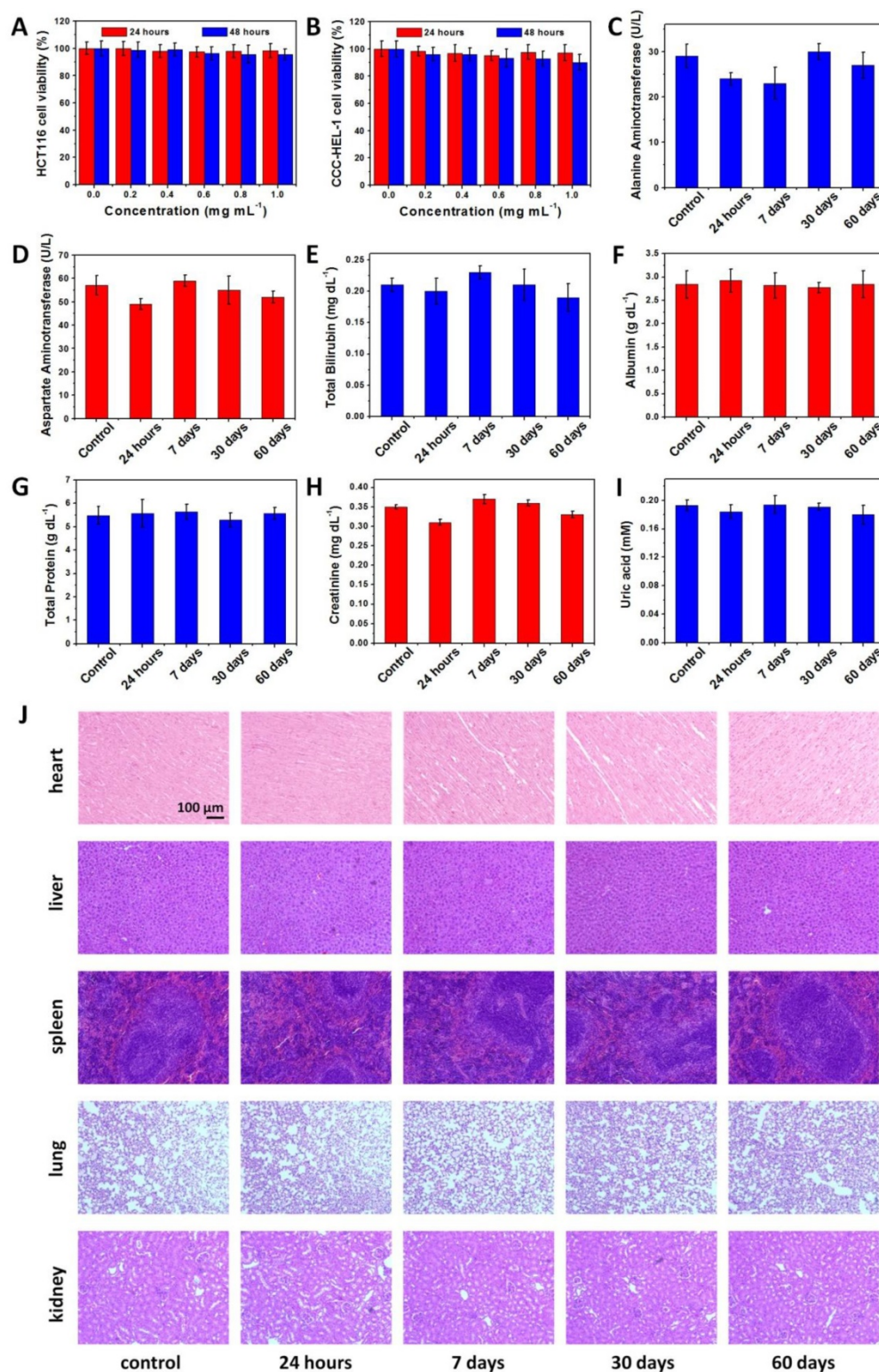


Figure 5. Toxicity of NaDyF₄:10%Nd-GA-Fe in vitro and in vivo. The viability of HCT116 A) and CCC-HEL-1 B) cells incubated with different concentrations NaDyF₄:10%Nd-GA-Fe within 24 and 48 hours. Serum biochemistry results obtained from mice injected with NaDyF₄:10%Nd-GA-Fe (20 mg kg⁻¹) different time post-injection (24 hours, 7 days, 30 days, and 60 days) and mice receiving no injection (control). C) ALT (alanine aminotransferase); D) AST (aspartate amino transferase); E) TBIL, total bilirubin; F) ALB, albumin; G) TP, total protein; H) CREA, creatinine; I) UA, uric acid. J) H&E-stained tissue sections from mice injected with NaDyF₄:10%Nd-GA-Fe (20 mg kg⁻¹) different time post-injection (24 hours, 7 days, 30 days, and 60 days) and mice receiving no injection (control). Tissues were harvested from heart, liver, spleen, lung, and kidney.

Synthesis of the OA-coated NaDyF₄:x%Nd (x = 2.5, 5, 10, 20)

In a typical experiment, a mixture of 1 mM LnCl₃ (Ln: Nd, Dy), 6 mL OA, and 15 mL ODE were added into a 100 mL three-necked flask. Under the vacuum, the mixture was heated to 160°C to form a clear solution, and then cooled to room temperature. After the solution cooling down, NaOH (0.025 mmol, 0.1 g) and NH₄F (0.04 mmol, 0.1481 g) were added into the flask directly and stirred for 30 min. The solution was slowly heated with gently stirred, degassed at 100°C, and then heated to 300°C and maintained for 1 h under the argon atmosphere. After the solution was cooled naturally, the nanoparticles were washed with ethanol/cyclohexane (1:1 v/v) several times and dispersed in cyclohexane¹⁵.

Synthesis of the GA-coated NaDyF₄:x%Nd (x = 2.5, 5, 10, 20)

Ligand-free NaDyF₄:x%Nd (x = 2.5, 5, 10, 20) was obtained by a reported method⁴⁷. In a typical experiment, 5 mL of dichloromethane solution of NOBF₄ (0.01 M) was dropped into 5 mL of OA-coated NaDyF₄:x%Nd (x = 2.5, 5, 10, 20) dispersion in hexane (~5 mg mL⁻¹) at room temperature. Then, the ligand-free NaDyF₄:x%Nd (x = 2.5, 5, 10, 20) were washed with ethanol several times and dispersed in DI water. Ligand-free NaDyF₄:x%Nd (x = 2.5, 5, 10, 20) were then dispersed in a saturated solution of GA as the host reagent, being ultrasonically treated for 10 min at room temperature. The resultant mixture was separated to obtain GA-coated NaDyF₄:x%Nd (x = 2.5, 5, 10, 20) (NaDyF₄:x%Nd-GA) *via* centrifugation and washed with DI water several times to remove the extra GA.

Synthesis of the NaDyF₄:10%Nd-GA-Fe

NaDyF₄:10%Nd-GA-Fe were fabricated by simply mixing 5 mL 1.0 mg mL⁻¹ FeCl₃ with 10 mL 1 mg mL⁻¹ NaDyF₄:10%Nd-GA suspension (pH = 7.4) at room temperature. After vigorous stirring for another 50 min, the resulting colloidal solution was centrifuged and washed with DI water for several times.

Photothermal properties measurement

Photothermal imaging system was designed as described in previously literature⁴⁸. To investigate the photothermal effect, NaDyF₄:x%Nd (x = 2.5, 5, 10, 20) and NaDyF₄:10%Nd-GA-Fe suspensions (200 µg mL⁻¹) were poured in specimen bottles (total volume of 2.0 mL), irradiated by continuous-wave diode NIR laser with a center wavelength of 808 nm and output power of 0-1.5 W cm⁻² for 2 min or 6 min. The temperature was measured by a digital thermometer with a

thermo couple probe every 0.133 s. The photothermal images of NaDyF₄:x%Nd (x = 2.5, 5, 10, 20) and NaDyF₄:10%Nd-GA-Fe in solution were obtained using FLIR E40 equipment running on FLIR tools systems.

In vivo NIR II DCL imaging

The mice were scanned before and after the administration of contrast agent. The mice were injected with the solution of NaDyF₄:10%Nd-GA-Fe intravenously (10 mg per kg body weight of mouse) and applied to NIR II DCL imaging, which was performed with a modified DCL *in vivo* imaging system designed as described in previously literature³⁴. *In vivo* NIR II DCL signals were collected at 1060 ± 12 nm. NaDyF₄:10%Nd-CA-Fe was used for comparison.

Oxidation stress study

Singlet oxygen sensor green reagent (SOSG) solution (5 mL, 0.1 mM; molecular probes) was added to the medium containing HCT116 cells, NaDyF₄:10%Nd-GA-Fe incubated HCT116 cells, CCC-HEL-1 cells, and NaDyF₄:10%Nd-GA-Fe incubated CCC-HEL-1 cells. The fluorescence intensity of SOSG was determined at 531 nm with an excitation wavelength of 488 nm. Fluorescent measurements were obtained using a fluorescence spectrophotometer (Hitachi F-7000).

Supplementary Material

Supplementary experiment section and figures.
<http://www.thno.org/v07p4217s1.pdf>

Acknowledgements

The authors thank the funding of National Natural Science Foundation of China (21301121), Beijing talent foundation outstanding young individual project (2015000026833ZK02), and Youth innovative research team of Capital Normal University, and Opening Project of Shanghai Key Laboratory of Magnetic Resonance.

Competing Interests

The authors have declared that no competing interest exists.

References

- [1] Chen G, Roy I, Yang C, et al. Nanochemistry and Nanomedicine for Nanoparticle-based Diagnostics and Therapy. *Chem Rev.* 2016; 116:2826-2885.
- [2] Auzel F. Upconversion and Anti-stokes Processes with f and d Ions in Solids. *Chem Rev.* 2004; 104:139-173.
- [3] Li XM, Zhang F, Zhao DY. Lab on Upconversion Nanoparticles: Optical Properties and Applications Engineering via Designed Nanostructure. *Chem Soc Rev.* 2015; 44:1346-1378.
- [4] Zhang Y, Hong G, Zhang Y, et al. Ag₂S Quantum Dot: A Bright and Biocompatible Fluorescent Nanoprobe in the Second Near-Infrared Window. *ACS Nano.* 2012; 6:3695-3702.

- [5] Robinson JT, Hong G, Liang Y, et al. In Vivo Fluorescence Imaging in the Second Near-Infrared Window with Long Circulating Carbon Nanotubes Capable of Ultrahigh Tumor Uptake. *J Am Chem Soc.* 2012; 134:10664-10669.
- [6] Kim D, Lee N, Park YI, et al. Recent Advances in Inorganic Nanoparticle-Based NIR Luminescence Imaging: Semiconductor Nanoparticles and Lanthanide Nanoparticles. *Bioconjugate Chem.* 2017; 28:115-123.
- [7] Zhang Y, Yu Z, Li J, et al. Ultrasmall-Superbright Neodymium-Upconversion Nanoparticles via Energy Migration Manipulation and Lattice Modification: 808 nm-Activated Drug Release. *ACS Nano.* 2017; 11:2846-2857.
- [8] Yang G, Yang D, Yang P, et al. A Single 808 nm Near-Infrared Light-Mediated Multiple Imaging and Photodynamic Therapy Based on Titania Coupled Upconversion Nanoparticles. *Chem Mater.* 2015; 27:7957-7968.
- [9] Zhou J, Liu Q, Feng W, et al. Upconversion Luminescent Materials: Advances and Applications. *Chem Rev.* 2015; 115:395-465.
- [10] Zhu XJ, Su QQ, Feng W, et al. Anti-Stokes Shift Luminescent Materials for Bio-applications. *Chem Soc Rev.* 2017; 46:1025-1039.
- [11] Lee N, Yoo D, Ling D, et al. Iron Oxide Based Nanoparticles for Multimodal Imaging and Magneto-responsive Therapy. *Chem Rev.* 2015; 115:10637-10689.
- [12] Yang L, Ma L, Xin J, et al. Composition Tunable Manganese Ferrite Nanoparticles for Optimized T₂ Contrast Ability. *Chem Mater.* 2017; 29:3038-3047.
- [13] Zhang X, Blasiak B, Marengo AJ, et al. Design and Regulation of NaHoF₄ and NaDyF₄ Nanoparticles for High-Field Magnetic Resonance Imaging. *Chem Mater.* 2016; 28:3060-3072.
- [14] Zhou J, Lu ZG, Shan G, et al. Gadolinium Complex and Phosphorescent Probe-modified NaDyF₄ Nanorods for T₁- and T₂-weighted MRI/CT/phosphorescence Multimodality Imaging. *Biomaterials.* 2014; 35:368-377.
- [15] Liu YX, Guo QW, Zhu XJ, et al. Optimization of Prussian Blue Coated NaDyF₄:x%Lu Nanocomposites for Multifunctional Imaging-Guided Photothermal Therapy. *Adv Funct Mater.* 2016; 26:5120-5130.
- [16] Melamed JR, Edelstein RS, Day ES. Elucidating the Fundamental Mechanisms of Cell Death Triggered by Photothermal Therapy. *ACS Nano.* 2015; 9:6-11.
- [17] Cheng L, Wang C, Feng LZ, et al. Functional Nanomaterials for Phototherapies of Cancer. *Chem Rev.* 2014; 114:10869-10939.
- [18] Huang XQ, Tang SF, Mu XL, et al. Freestanding Palladium Nanosheets with Plasmonic and Catalytic Properties. *Nat Nanotechnol.* 2011; 6:28-32.
- [19] Wang J, Liu J, Liu Y, et al. Gd-Hybridized Plasmonic Au-Nanocomposites Enhanced Tumor-Interior Drug Permeability in Multimodal Imaging-Guided Therapy. *Adv Mater.* 2016; 28:8950-8958.
- [20] Pang B, Zhao Y, Luehmann H, et al. ⁶⁴Cu-Doped PdCu@Au Tripods: A Multifunctional Nanomaterial for Positron Emission Tomography and Image-Guided Photothermal Cancer Treatment. *ACS Nano.* 2016; 10:3121-3131.
- [21] Ghosh S, Avellini T, Petrelli A, et al. Colloidal CuFe₂S₂ Nanocrystals: Intermediate Fe d-Band Leads to High Photothermal Conversion Efficiency. *Chem Mater.* 2016; 28:4848-4858.
- [22] Mou J, Lin TQ, Huang FQ, et al. A New Green Titania with Enhanced NIR Absorption for Mitochondria-Targeted Cancer Therapy. *Theranostics.* 2017; 7:1531-1542.
- [23] Song XR, Wang X, Yu SX, et al. Co₂Se₃ Nanoplates as a New Theranostic Platform for Photoacoustic/Magnetic Resonance Dual-Modal-Imaging-Guided Chemo-Photothermal Combination Therapy. *Adv Mater.* 2015; 27:3285-3291.
- [24] Liu YX, Zhang G, Guo QW, et al. Artificially Controlled Degradable Inorganic Nanomaterial for Cancer Theranostics. *Biomaterials.* 2017; 112:204-217.
- [25] Liu YX, Li LY, Guo QW, et al. Novel Cs-based Upconversion Nanoparticles as Dual-modal CT And UCL Imaging Agents For Chemo-photothermal Synergistic Therapy. *Theranostics.* 2016; 6:1491-1505.
- [26] Cai X, Jia X, Gao W, et al. A Versatile Nanotheranostic Agent for Efficient Dual-Mode Imaging Guided Synergistic Chemo-Thermal Tumor Therapy. *Adv Funct Mater.* 2015; 25:2520-2529.
- [27] Wang Y, Yang T, Ke H, et al. Smart Albumin-Biomaterialized Nanocomposites for Multimodal Imaging and Photothermal Tumor Ablation. *Adv Mater.* 2015; 27:3874-3882.
- [28] Cao Y, Dou J, Zhao N, et al. Highly Efficient NIR-II Photothermal Conversion Based on an Organic Conjugated Polymer. *Chem Mater.* 2017; 29:718-725.
- [29] Li LY, Liu YX, Hao PL, et al. PEDOT Nanocomposites Mediated Dual-modal Photodynamic and Photothermal Targeted Sterilization in Both NIR I and II Window. *Biomaterials.* 2015; 41:132-140.
- [30] Liang XL, Li YY, Li XD, et al. PEGylated Polypyrrole Nanoparticles Conjugating Gadolinium Chelates for Dual-Modal MRI/Photoacoustic Imaging Guided Photothermal Therapy of Cancer. *Adv Funct Mater.* 2015; 25:1451-1462.
- [31] Ju E, Dong K, Liu Z, et al. Tumor Microenvironment Activated Photothermal Strategy for Precisely Controlled Ablation of Solid Tumors upon NIR Irradiation. *Adv Funct Mater.* 2015; 25:1574-1580.
- [32] Hu DH, Zhang JN, Gao GH, et al. Indocyanine Green-Loaded Polydopamine-reduced Graphene Oxide Nanocomposites with Amplifying Photoacoustic and Photothermal Effects for Cancer Theranostics. *Theranostics.* 2016; 6:1043-1052.
- [33] Kang S, Lee J, Ryu S, et al. Gold Nanoparticle/Graphene Oxide Hybrid Sheets Attached on Mesenchymal Stem Cells for Effective Photothermal Cancer Therapy. *Chem Mater.* 2017; 29:3461-3476.
- [34] Zhu XJ, Feng W, Chang J, et al. Temperature-feedback Upconversion Nanocomposite for Accurate Photothermal Therapy at Facile Temperature. *Nat Commun.* 2016; 7:10437.
- [35] Porcu EP, Salis A, Gavini E, et al. Indocyanine Green Delivery Systems for Tumour Detection and Treatments. *Biotechnol Adv.* 2016; 34:768-789.
- [36] Song GS, Hao J, Liang C, et al. Degradable Molybdenum Oxide Nanosheets with Rapid Clearance and Efficient Tumor Homing Capabilities as a Therapeutic Nanoplatfrom. *Angew Chem Int Ed.* 2016; 55:2122-2126.
- [37] Yu MX, Zhou C, Liu L, et al. Interactions of Renal-Clearable Gold Nanoparticles with Tumor Microenvironments: Vasculature and Acidity Effects. *Angew Chem Int Ed.* 2017; 56:4314-4319.
- [38] Wang F, Wang J, Liu XG. Direct Evidence of a Surface Quenching Effect on Size-Dependent Luminescence of Upconversion Nanoparticles. *Angew. Chem. Int. Ed.* 2010, 49:7456-7460.
- [39] Tromsdorf UI, Bigall NC, Kaul MG, et al. Size and Surface Effects on the MRI Relaxivity of Manganese Ferrite Nanoparticle Contrast Agents. *Nano Lett.* 2007; 7:2422-2427.
- [40] Chen H, Shao L, Ming T, et al. Understanding the Photothermal Conversion Efficiency of Gold Nanocrystals. *Small.* 2010; 6:2272-2280.
- [41] Chen GY, Ohulchanskyy TY, Liu S, et al. Core/Shell NaGdF₄:Nd³⁺/NaGdF₄ Nanocrystals with Efficient Near-Infrared to Near-Infrared Downconversion Photoluminescence for Bioimaging Applications. *ACS Nano.* 2012; 6:2969-2977.
- [42] Zeng J, Cheng M, Wang Y, et al. pH-Responsive Fe(III)-Gallic Acid Nanoparticles for In Vivo Photoacoustic-Imaging-Guided Photothermal Therapy. *Adv Healthcare Mater.* 2016; 5:772-780.
- [43] Dou R, Du Z, Bao T, et al. The Polyvinylpyrrolidone Functionalized rGO/Bi₂S₃ Nanocomposite as a Near-Infrared Light-responsive Nanovehicle for Chemo-photothermal Therapy of Cancer. *Nanoscale.* 2016; 8:11531-11542.
- [44] Ren Q, Li B, Peng Z, et al. SnS Nanosheets for Efficient Photothermal Therapy. *New J Chem.* 2016; 40:4464-4467.
- [45] Yao C, Wang P, Li XM, et al. Near-Infrared-Triggered Azobenzene-Liposome/Upconversion Nanoparticle Hybrid Vesicles for Remotely Controlled Drug Delivery to Overcome Cancer Multidrug Resistance. *Adv Mater.* 2016; 28:9341-9348.
- [46] Smith BR, Gambhir SS. Nanomaterials for In Vivo Imaging. *Chem Rev.* 2017; 117:901-986.
- [47] Dong AG, Ye XC, Chen J, et al. A Generalized Ligand-Exchange Strategy Enabling Sequential Surface Functionalization of Colloidal Nanocrystals. *J Am Chem Soc.* 2010; 133:998-1006.
- [48] Zhou J, Lu ZG, Zhu XJ, et al. NIR Photothermal Therapy Using Polyaniline Nanoparticles. *Biomaterials.* 2013; 34:9584-9592.